Ocean Sci., 13, 1017–1033, 2017
https://doi.org/10.5194/os-13-1017-2017

Ocean Science
Open Access

Submesoscale CO_2 variability across an upwelling front off Peru

Eike E. Köhn[1], **Sören Thomsen**[1], **Damian L. Arévalo-Martínez**[1], **and Torsten Kanzow**[2,3]

[1]GEOMAR Helmholtz Centre for Ocean Research Kiel, Kiel, Germany
[2]Alfred Wegener Institute Helmholtz Centre for Polar and Marine Research, Bremerhaven, Germany
[3]Department 1 of Physics and Electrical Engineering, University of Bremen, Bremen, Germany

Correspondence to: Eike E. Köhn (ekoehn@geomar.de)

Received: 17 May 2017 – Discussion started: 22 June 2017
Revised: 4 October 2017 – Accepted: 10 October 2017 – Published: 4 December 2017

Abstract. As a major source for atmospheric CO_2, the Peruvian upwelling region exhibits strong variability in surface fCO_2 on short spatial and temporal scales. Understanding the physical processes driving the strong variability is of fundamental importance for constraining the effect of marine emissions from upwelling regions on the global CO_2 budget. In this study, a frontal decay on length scales of $\mathcal{O}(10\,\text{km})$ was observed off the Peruvian coast following a pronounced decrease in down-frontal (equatorward) wind speed with a time lag of 9 h. Simultaneously, the sea-to-air flux of CO_2 on the inshore (cold) side of the front dropped from up to 80 to 10 $\text{mmol m}^{-2}\text{ day}^{-1}$, while the offshore (warm) side of the front was constantly outgassing at a rate of 10–20 $\text{mmol m}^{-2}\text{ day}^{-1}$. Based on repeated ship transects the decay of the front was observed to occur in two phases. The first phase was characterized by a development of coherent surface temperature anomalies which gained in amplitude over 6–9 h. The second phase was characterized by a disappearance of the surface temperature front within 6 h. Submesoscale mixed-layer instabilities were present but seem too slow to completely remove the temperature gradient in this short time period. Dynamics such as a pressure-driven gravity current appear to be a likely mechanism behind the evolution of the front.

1 Introduction

Although the ocean generally acts as a net sink for atmospheric CO_2 (Takahashi et al., 2009), most low-latitude eastern boundary upwelling systems (EBUSs) are natural sources of CO_2 to the atmosphere (Chavez et al., 2007; Capone and Hutchins, 2013; Gruber, 2015). The distribution of CO_2 in such areas is complex and results from the interaction between cooling/warming at the surface, upwelling and mixing, biological activity, and riverine carbon and nutrient input (Laruelle et al., 2014; Gruber, 2015). As one of the four major EBUSs, the Peruvian upwelling region is an important area for the exchange of climate relevant gases (e.g., CO_2, N_2O) between the ocean and the atmosphere (Friederich et al., 2008; Arévalo-Martínez et al., 2015). Hence, quantification of sea-to-air fluxes of CO_2 as well as their spatial and temporal variability in the Peruvian upwelling region is essential for constraining the global budget of CO_2 in a changing climate.

High variability of surface CO_2 in the Peruvian upwelling region is observed over short timescales $\mathcal{O}$(hours–days) and space $\mathcal{O}$(km) scales driven by both biological and physical processes (Friederich et al., 2008). The sharp lateral temperature gradient, separating the newly upwelled cold water from warm surface waters further offshore, allows for pronounced frontal processes, which manifest themselves in eddies and filaments (Penven et al., 2005; Chaigneau et al., 2008; McWilliams et al., 2009; Colas et al., 2012; Thomsen et al., 2016a). These submesoscale features, which go along with Rossby numbers $Ro = \mathcal{O}(1)$, can develop strong vertical velocities in the upper ocean layer. Thus, surface fronts may enable the exchange of large amounts of heat and gas between the atmosphere and the subsurface ocean (Ferrari, 2011). However, submesoscale frontal processes are difficult to observe due to their small spatial and temporal scales. At the same time the importance of these dynamics for physical–biogeochemical coupling has been put forward by model studies, e.g., by altering the vertical transports of nutrients and organic carbon (Lapeyre and Klein, 2006; Lévy et al., 2012).

Published by Copernicus Publications on behalf of the European Geosciences Union.

The link between the surface CO_2 distribution and the (sub)mesoscale flow field was studied in the open ocean of the northeast Atlantic by Merlivat et al. (2009), using both underway and Lagrangian surface drifter measurements. During the measurement period, the study area was characterized by weak eddy kinetic energy. Still, submesoscale variability with large-amplitude variations of surface CO_2 concentrations on horizontal length scales of $\mathcal{O}(10\,\mathrm{km})$ was observed. This variability was successfully reproduced by the modeling study of Resplandy et al. (2009) but it does not seem to have a major effect on the model's overall CO_2 budget. The influence of submesoscale variability on the overall CO_2 budget might be stronger in the case of EBUS due to the ubiquitous existence of sharp fronts and filaments, i.e., in the case of a highly energetic (sub)mesoscale flow field (McWilliams et al., 2009; Colas et al., 2012). However, so far no observations are available which describe the variability on the submesoscale off Peru.

In this study repeated measurements of CO_2 and physical properties across the upwelling front off Peru near 14° S are presented (see Fig. 1 for the large-scale setting of the experiment). Throughout the 2-day experiment, we observed short-term fluctuations (timescales on $\mathcal{O}$(hours)) of the surface temperature and velocity field. Simultaneously, surface CO_2 sea-to-air fluxes showed pronounced changes, implicating the importance of these timescales for the ocean–atmosphere gas exchange. The goals of this paper are to (1) document the high-frequency variability across the upwelling front and (2) discuss possible physical driving mechanisms, improving our current understanding of the variability of surface CO_2 in the Peruvian upwelling region.

This paper is structured as follows: in Sect. 2 we present the experiment, the physical and biogeochemical data sets used for this study, and the methods employed for their analysis. Section 3 contains a description of the initial state of the front. Observations from the following frontal evolution are presented in Sect. 4. Subsequently, the changes across the temperature front are analyzed in the context of various possible underlying dynamics, such as surface heating (Sect. 4.1), Ekman buoyancy fluxes (Sect. 4.2), submesoscale mixed-layer instabilities (Sect. 4.3), or pressure-driven gravity currents (Sect. 4.4). In Sect. 5 these mechanisms are compared with respect to their associated buoyancy fluxes. Section 6 contains a discussion of the different mechanisms which possibly drive the observed variability. The conclusions drawn from this study follow in Sect. 7.

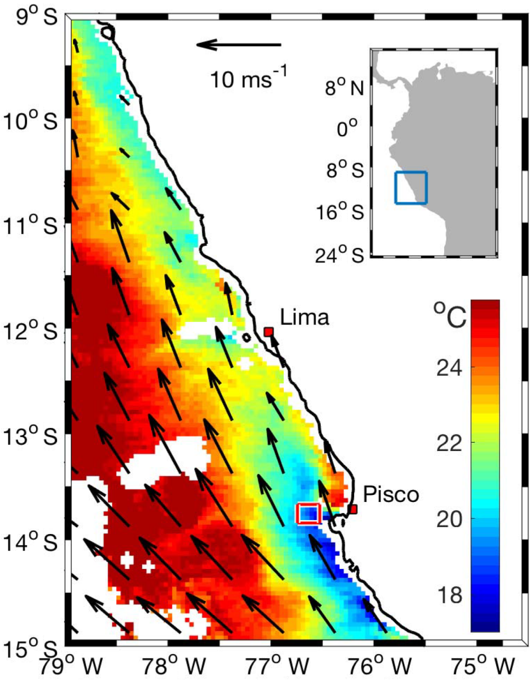

Figure 1. MODIS SST (color) and ASCAT (Advanced Scatterometer) wind field (arrows) off the Peruvian coast on 16 February 2013. The small red box shows the study region off Pisco.

2 Data and methods

2.1 Hydrographic and meteorological measurements

Near 14° S and 76°30′ W the Peruvian upwelling region is characterized by a strong quasi-permanent upwelling cell (Fig. 1). The corresponding "upwelling front" was intensively sampled from 16 to 18 February during the RV *Meteor* cruise M93 in February/March 2013. The field work was carried out within the framework of the Collaborative Research Centre SFB754 Climate-Biogeochemistry Interactions in the Tropical Ocean project (www.sfb754.de). The experiment's procedure was as follows: prior to the main experiment, a conductivity, temperature, and pressure (CTD) section (transect A, black squares in Fig. 2) was conducted on 16 February from 10:00 to 15:00 (time in UTC unless stated differently) to document the horizontal circulation and the initial vertical distribution of temperature, salinity, dissolved oxygen (O_2), and chlorophyll *a* (Chl *a*) across the front. Starting on 17 February at 04:00, the upwelling front was mapped in seven ∼ 10 km long zonal transects. These were conducted from north to south at 1.8 km spacing (Fig. 2). Each zonal transect took about 45 min. From the highest and lowest surface temperature recorded, a cross-frontal axis was estimated. Subsequently, 17 cross-frontal transects were conducted along this axis to study the variability of the front on timescales of several hours. Among these, two high-resolution temperature transects B and C were conducted as cross-frontal transects 12 and 14. The high-resolution transects took 4.5 h each to complete, while a regular cross-frontal transect was completed in 40 min. The cross-frontal transects were conducted within a 1.8 km wide corridor on three parallel tracks (Fig. 2).

The physical state of the upwelling front is mainly deduced from underway temperature, wind, and velocity mea-

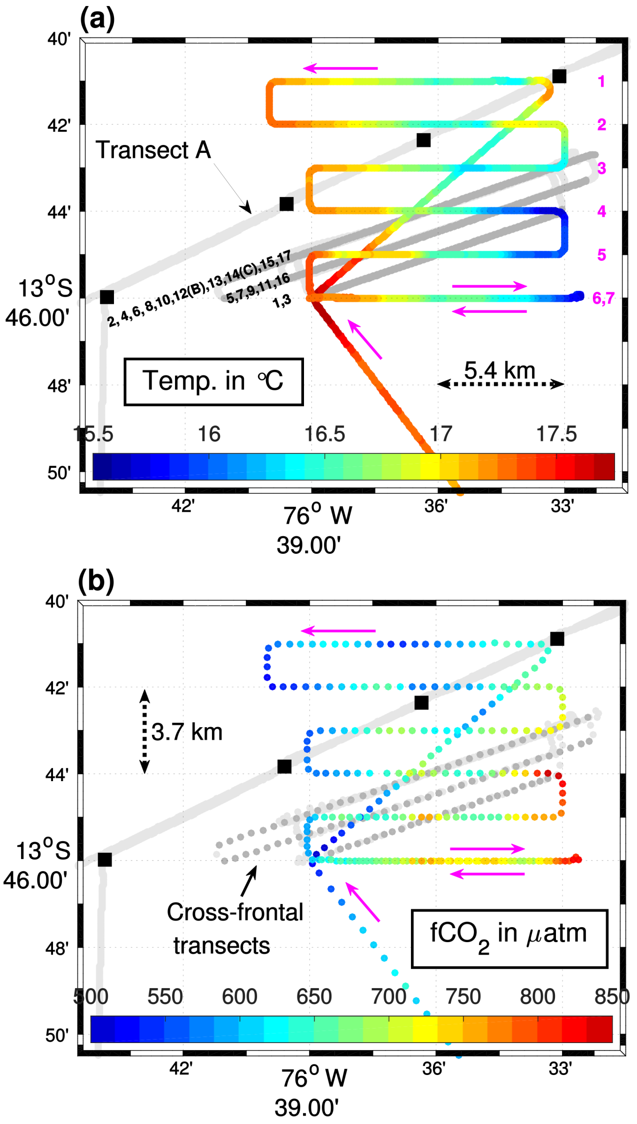

Figure 2. Sampling map of underway temperature **(a)** and $f\mathrm{CO}_2$ **(b)** along the cruise track. The solid light grey line shows the CTD section (transect A) conducted prior to the seven zonal transects, with black squares indicating CTD stations. The 17 cross-frontal transects are marked by the dark grey lines **(a)** and dots **(b)**. The black numbers in **(a)** correspond to the cross-frontal transects. Transects 12 and 14 correspond to the high-resolution subsurface temperature transects B and C. Magenta arrows show the direction of the ship's track and magenta numbers label the zonal transects. The area presented in both panels is depicted as a red square in Fig. 1.

surements. Underway temperature was measured with the thermosalinograph using an external SBE-38 digital thermometer at 3.5–4 m depth at the vessel's port-side bow. Temperature data were gathered at 0.1 Hz and filtered with a second-order low-pass Butterworth filter with a cutoff period of 250 s to remove the effect due to high frequent ship movements. Wind velocity and direction were measured at a height of 35.3 m above the sea surface at a temporal resolution of 60 s. The surface wind stress was estimated from these measurements following Smith (1988). Underway ocean current velocity measurements with a vertical resolution of 4 m were obtained from a vessel-mounted 75 kHz acoustic Doppler current profiler (vmADCP). The shallowest vmADCP-based current velocities were obtained in a bin centered at 11 m below the sea surface. The data were averaged in 1 min ensembles and smoothed using a 3 min running mean. A 16.56° counterclockwise rotation is applied to transform the measured currents into along-front and cross-front velocities (note the frontal orientation in Fig. 2). As a result positive cross-front velocities are directed towards the coast and positive along-front velocities indicate an equatorward flow. Underway measurements of salinity are unavailable as the thermosalinograph's conductivity sensor failed to produce consistent results. Likewise, temperature and vmADCP measurements taken during periods of highly variable vessel speed and heading proved to be unreliable due to the influence of the ship. Thus, current measurements immediately before and after CTD stations are neglected in the following data analysis. During the analyzed transects the vessel speed was held at approximately constant 4 m s^{-1} in order to achieve high-quality ADCP data.

Hydrographic data *below* the surface were obtained from lowered CTD measurements. These are arranged in transect A consisting of four shallow CTD profiles located 7 km apart (black squares in Fig. 2). The CTD was equipped with a fluorometer and an oxygen sensor, allowing for Chl *a* and O$_2$ measurements. A detailed description of the data processing, including the calibration of oxygen can be found in Thomsen et al. (2016b). As the Chl *a* concentrations measured by the WET Labs (USA) fluorometer did not differ significantly from Chl *a* concentrations determined from water samples (Meyer et al., 2017), no further calibration than the factory calibration was applied to the fluorometer data (see Loginova et al., 2016, for details). In order to obtain further subsurface hydrographic information, 53 temperature profiles organized in the two cross-frontal transects B and C with a horizontal resolution of 0.3–0.5 km were measured using the CTD sensors mounted on a microstructure profiler. During these measurements the speed of the vessel was reduced to about 0.75 m s^{-1}.

Surface diabatic heating was calculated from underway measurements as $Q_{\mathrm{net}} = Q_{\mathrm{lw}} + Q_{\mathrm{sw}} + Q_{\mathrm{sh}} + Q_{\mathrm{lh}}$, i.e., the sum of longwave and shortwave radiation as well as sensible and latent heat fluxes. Net shortwave radiation into the ocean was estimated using underway measurements of downward shortwave radiation under consideration of the surface albedo effect (Payne, 1972). Net longwave radiation into the ocean was calculated as the difference between the measured downward longwave radiation and outgoing longwave radiation estimated using the Stefan–Boltzman law (with an emissivity of 0.985) applied to the thermosalinograph's temperature measurements. Latent and sensible heat fluxes along the cruise track were calculated using bulk formulae including the Webb correction to the latent heat flux (Fairall et al., 1996b). During the experiment an average flux of latent heat of 20 $W\,m^{-2}$ *into* the ocean was observed. This coincided with high relative humidity and partially foggy conditions. Neither a cool-skin nor a warm-skin correction is applied to the thermosalinograph's temperature measurements. A cool skin would primarily form during nighttime, but is estimated to be on average less than 0.02 K cooler than the temperature measured by the thermosalinograph (Fairall et al., 1996a). A potentially larger warm-skin correction, which would increase outgoing longwave radiation mainly during periods of strong insolation, is not applied. This error in heat flux is, however, small compared to the dominant heat flux related to shortwave radiation during daytime.

The large-scale sea surface temperature (SST) was retrieved from NASA's OceanColor project as daily satellite MODIS Aqua and Terra SST data (https://oceancolor.gsfc.nasa.gov/). For the large-scale wind field, Advanced Scatterometer (ASCAT) wind data (Bentamy and Fillon, 2012) were taken from the Asia-Pacific Data-Research Center at the University of Hawai'i (http://apdrc.soest.hawaii.edu/datadoc/ascat.php). The spatial resolution of SST was 4 km, while the wind data were available on a 0.25° grid. The ubiquitous presence of clouds during the main experiment period hindered the extensive use of remote sensing data sets.

2.2 Underway CO_2 measurements

CO_2 measurements were conducted by means of an underway system as described in Arévalo-Martínez et al. (2013). Seawater was drawn on board from a depth of about 6 m by means of a LOWARA submersible pump which was installed at the ship's moon pool. Atmospheric measurements were carried out every 6 h by means of an AirCadet pump (Thermo Scientific Inc., USA) which continuously brought air from 35 m height into the laboratory. Likewise, control measurements of standard gas mixtures with 201.0 and 602.4 ppm CO_2 were used in order to post-correct our data due to instrumental drift. The gas standards were prepared at Deuste Steininger GmbH (Mühlhausen, Germany) and were calibrated at the Max Planck Institute for Biogeochemistry (Jena, Germany) against the World Meteorological Organization standard scale. CO_2 data calibration as well as computation of CO_2 fugacities (fCO_2) was done according to the guidelines from Dickson et al. (2007). We report all seawater and atmospheric CO_2 values as 1 min means. For this, we used a mean surface salinity from all CTD measurements of the M93 campaign (35.04), as salinity was not available from underway measurements. A change in the mean salinity by 1 leads to a mean offset of 0.0055 µatm and thus has small influence compared to temperature with an isochemical dependence of 15 $\mu atm\,{}^{\circ}C^{-1}$ (e.g., Körtzinger et al., 2000; Pierrot et al., 2009). The uncertainty of the CO_2 measurements was hence about ±2 µatm. The air–sea flux of CO_2 was computed by using $F = kK_0(fCO_{2sw} - fCO_{2air})$, where k is the air–sea gas exchange coefficient, calculated using the parameterization of Nightingale et al. (2000) with wind speeds standardized to 10 m height (Smith, 1988). K_0 is the solubility of CO_2 in seawater, calculated with the equations and coefficients from Weiss (1974) and Weiss and Price (1980), and fCO_{2sw} and fCO_{2air} are the fugacities of CO_2 in seawater and atmosphere, respectively. The strongest correlation between the underway temperature and fCO_2 measurements was found at a time lag of 4 min ($r = -0.86$) (Fig. 3), which is probably due to the travel time for the seawater from the uptake to the underway CO_2 sensor. Thus CO_2 fugacities and fluxes are corrected for this time lag.

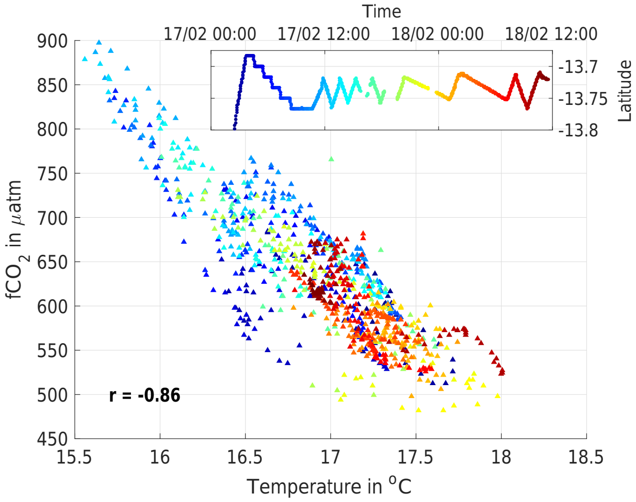

Figure 3. Correlation of surface temperature and fCO_2 during the main experiment. The fCO_2 values are corrected for a 4 min time lag. The correlation value r is given in the bottom left corner. Data points are color-coded by their time of measurement. The top right box shows an orientation as to when the data were measured during the experiment. The color-coding carries the same information as the time axis.

3 Physical and biogeochemical properties of the upwelling front

The experiment period can be divided into three different wind forcing regimes. The first regime is characterized by down-frontal (equatorward) winds with speeds above 10 $m\,s^{-1}$ (Fig. 4). It lasts from the beginning of the experiment including the CTD transect (Fig. 5) until 17 February, 11:00, i.e., right after the beginning of the cross-frontal transects. During this phase, the front is characterized by a strong cross-frontal surface temperature gradient of about 1 °C over 10 km (Fig. 6a). The CTD transect reveals the strong subsurface frontal signature in the temperature and salinity field (Fig. 5b, c). The mixed layer exhibits almost

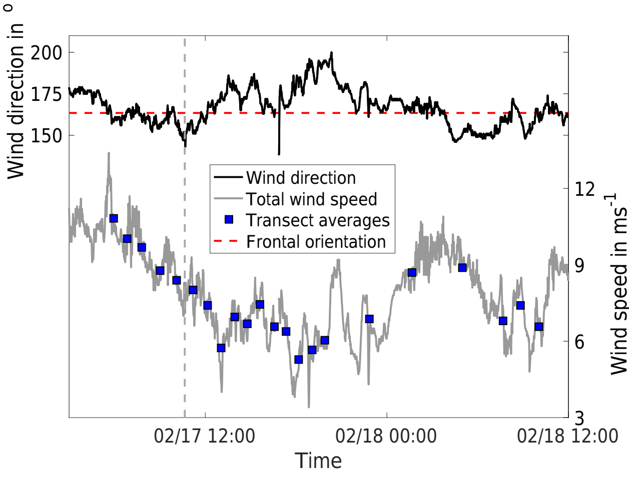

Figure 4. Time series of total wind speed (grey) and wind direction (black) from underway measurements at 35.3 m height. Blue rectangles show mean total wind speed for each zonal and cross-frontal transect. The dashed red line shows the (initial) frontal orientation deduced from the frontal mapping. The angle of 163.44° implicates the front running from south–southeast to north–northwest. The vertical dashed grey line indicates the transition from zonal to cross-frontal transects. Time is given in UTC.

vertical isopycnals and is estimated to be about 15 m deep, using a $\Delta T = 0.2\,°C$ criterion. The southward flowing Peru–Chile Undercurrent (PCUC) weakens from $\sim 20\,cm\,s^{-1}$ at 80 m depth towards the surface (Fig. 5a). The along-frontal velocity is low in the shallowest ADCP bin throughout the experiment (Fig. 7). As a result, lateral along-frontal advection is likely to play a minor role at the surface. In agreement with extensive upwelling of cold, nutrient-rich waters during the strong wind period the Chl *a* concentrations on the onshore side of the front were strongly enhanced with concentrations reaching $7\,\mu g\,L^{-1}$ in the mixed layer (Fig. 5e). Simultaneously, the subsurface O_2 minimum was drawn closer to the surface on the onshore side of the front (Fig. 5d). Concentrations below $100\,\mu mol\,kg^{-1}$ could be found at 15 m depth, and values dropped below $20\,\mu mol\,kg^{-1}$ already beneath ~ 40 m. Furthermore, a gradient in surface fCO_2 was discernible during the CTD transect (not shown) and during the zonal ship sections across the front (Fig. 2b), increasing from 600 µatm in offshore locations up to over 800 µatm on the onshore side of the front. During this period, peak sea-to-air CO_2 fluxes of over $80\,mmol\,m^{-2}\,day^{-1}$ are measured on the cold side of the front (Fig. 6d).

4 Cross-frontal changes after weakening of down-frontal winds

During the second wind period from 11:00 to 21:00 on 17 February the wind continues to blow in the down-frontal direction but drops to almost $5\,m\,s^{-1}$ (Fig. 4). During this period the clear surface temperature gradient signal is disturbed by coherent anomalies appearing at 50 km off the coast (Fig. 6b). These anomalies grow in amplitude and lead to a break up of the clear temperature gradient at around 20:00. At the same time the strong outgassing of CO_2 is reduced on the onshore side of the front (Fig. 6d), while surface fCO_2 values remain rather high until about 18:00 (Fig. 6c). At the beginning of the transition to the low wind speed period, a strong offshore directed velocity signal is observed close to the surface on the onshore side of the front (Fig. 7a). The velocity maximum of up to $15\,cm\,s^{-1}$ deepens with increasing distance from shore. During the wind minimum, maximum offshore velocities are found at 25–30 m depth, exceeding $20\,cm\,s^{-1}$ (Fig. 7c). At the same time, the along-frontal velocity field exhibits a slight reduction in vertical shear (Fig. 7b, d).

At about 21:00 on 17 February the along-frontal (equatorward) wind begins to increase again and reaches about $9\,m\,s^{-1}$, defining the beginning of the third wind regime. Initially, the surface temperature gradient vanishes and even reverses slightly, before strengthening again towards 18 February 09:00. Both high-resolution temperature transects (B and C) exhibit average mixed-layer depths of 3 and 5 m, respectively (Fig. 8). The sections show that temperature changes are not limited to the surface layer but reach about 40–50 m deep. While the temperature field in transect B exhibits a clear frontal structure, the isotherms are close to horizontal in transect C, with exception of undulations associated with internal waves propagating onshore (e.g., at km 46 in Fig. 8b). As a result, the mean cross-frontal velocity field shows no longer any clear offshore directed velocity signal (Fig. 7e). Also, the subsurface along-frontal (poleward) velocity maximum of the PCUC appears to be weaker (Fig. 7f). During this last phase the outgassing of CO_2 is at its minimum with fluxes of less than $20\,mmol\,m^{-2}\,day^{-1}$ despite the again increased wind speeds (Fig. 6d). fCO_2 remains at ~ 600 µatm during this phase and increases only slightly along the last two transects during which the front starts to reform.

Figure 3 shows the correlation of surface temperature and fCO_2 during the main experiment. The high negative correlation indicates the governing effect of temperature on the CO_2 field. In particular, during the beginning of the experiment the high fCO_2 values are only found on the cold side of the front. Towards the end of the experiment the clear correlation signal breaks up. The changes in temperature and fCO_2 are observed over the course of $\mathcal{O}$(hours), giving phytoplankton only a short time window to react. It is thus likely that physical processes are mainly responsible for the measured variability in surface fCO_2. In the following part of this study, we analyze the observed changes across the upwelling front in the context of physical processes that could be responsible for driving the observed fCO_2 variability.

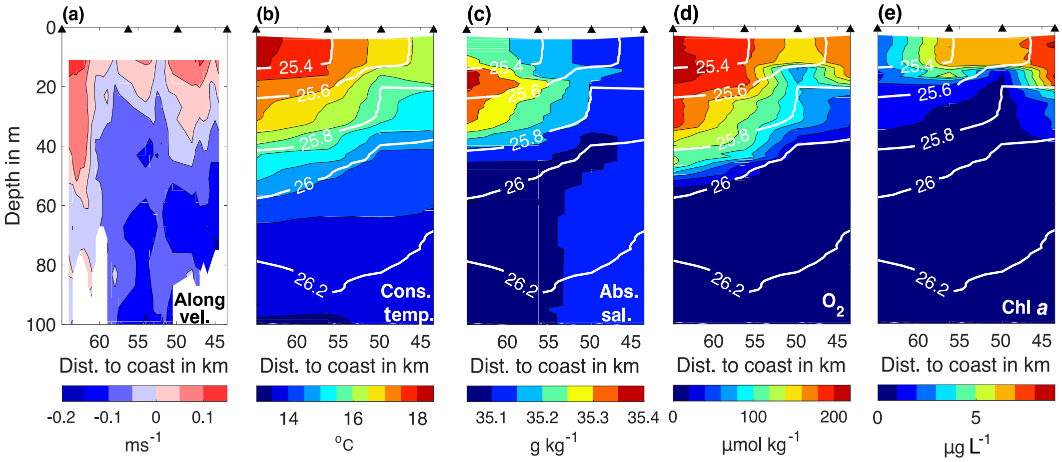

Figure 5. CTD transect across the upwelling front before the main experiment conducted on 16 February 2013. Measured quantities contain along-frontal current velocities **(a)**, conservative temperature **(b)**, absolute salinity **(c)**, O_2 **(d)**, and Chl *a* concentrations **(e)**. Isopycnals are given by white lines in **(b)**–**(e)**. Around CTD stations the along-frontal velocity is horizontally linearly interpolated.

4.1 Surface heat fluxes

The changes across the front are observed within a 24 h period. The wind begins to drop at 11:00 on 17 February (06:00 LT) and the temperature gradient fully vanishes 14 h later at 01:00 on 18 February (Fig. 6a). As this time period matches well with the diurnal cycle of solar insolation, it could be hypothesized that differential heating throughout the day causes the reduction of the cross-frontal temperature gradient. Figure 6f shows the diurnal cycle of net surface heat flux. During the zonal transects the ocean surface is heated on average by 50 W m^{-2}. Due to the absence of solar insolation, this heat flux is mostly maintained by latent and sensible heat fluxes *into* the ocean, overcoming the ocean's weak heat loss caused by outgoing long wave radiation (individual heat flux components not shown). At around 12:00 (07:00 LT) the net heat flux into the ocean begins to strengthen, associated with an intensification of solar insolation. During the fourth and the beginning of the fifth cross-frontal transect the heat flux into the ocean is hampered due to irregularities in the incoming shortwave radiation. The net heat flux reaches its peak of 1010 W m^{-2} at 18:00 (13:00 LT) and reduces subsequently. From 23:00 (18:00 LT) onwards, the net heat flux fluctuates around 0 W m^{-2}. During the last cross-frontal transects the surface is continuously cooled by less than 50 W m^{-2}. During the phase of strongest heating, the heat flux shows only small lateral differences of mostly less than 50 W m^{-2} across the temperature front. Furthermore, no clear pattern of slightly stronger heating on the cold side of the front is discernible. As a result, a uniform warming of the surface waters is expected. Sectional averaging of the first 13 cross-frontal transects, corresponding to the time period of incoming solar radiation, shows an increase of the transects' mean temperature of 0.8 °C. From $\Delta Q = \rho_r c_p V \Delta T$ with the reference density $\rho_r = 1035\,\mathrm{kg\,m^{-3}}$ and a heat capacity $c_p = 4000\,\mathrm{J\,kg^{-1}\,m^{-3}}$ it can be roughly estimated that over the same time period of 14.5 h the average net heat flux causes a warming of a surface water column of volume V with unit area and 10 m depth by 0.6 °C. Thus, the background temperature increase is most likely linked to the surface heat fluxes. The small-scale temperature anomalies develop during the phase of strong heating (Fig. 6b). Using the same calculation as above, the maximum heat flux of 1010 W m^{-2} can warm the surface water by almost 0.1 °C h^{-1}. Even though this roughly corresponds to the amplitude of the temperature anomalies, the lateral homogeneity of the net surface heat flux prohibits attributing the development of the anomalies to surface heating.

The temperature front finally vanishes during a phase of almost no net surface heat flux. The high-resolution temperature transects B and C (Fig. 8) show that during this phase, cooling takes place on the offshore side of the front, while the onshore side is significantly warmed over a period of 6 h. On the onshore side, temperature changes of ∼ 2 °C occur up to ∼ 40 m depth. A heat flux of ∼ 3800 W m^{-2} is required to heat a water column of 40 m by 0.5 °C using the rough estimate above. Likewise, comparably strong cooling is required on the offshore side of the front in order to explain the observed temperature changes. Neither the two heat fluxes nor the associated strong cross-frontal gradient are within the range of the observed values.

The net surface heat flux can be converted into a vertical buoyancy flux following $\langle w'b' \rangle_{Q_{\mathrm{net}}} = \alpha g Q_{\mathrm{net}}/(\rho c_p)$, where w' is the vertical velocity anomaly, b' is the buoyancy anomaly, g is the gravitational acceleration, and α is the thermal expansion coefficient. Due to the lack of data, the calculation of the surface density ρ requires an assumption about the salinity. The initial CTD section shows a surface salinity varying between 35.1 and 35.2 (Fig. 5c). Thus, the surface water density ρ is calculated using a constant salin-

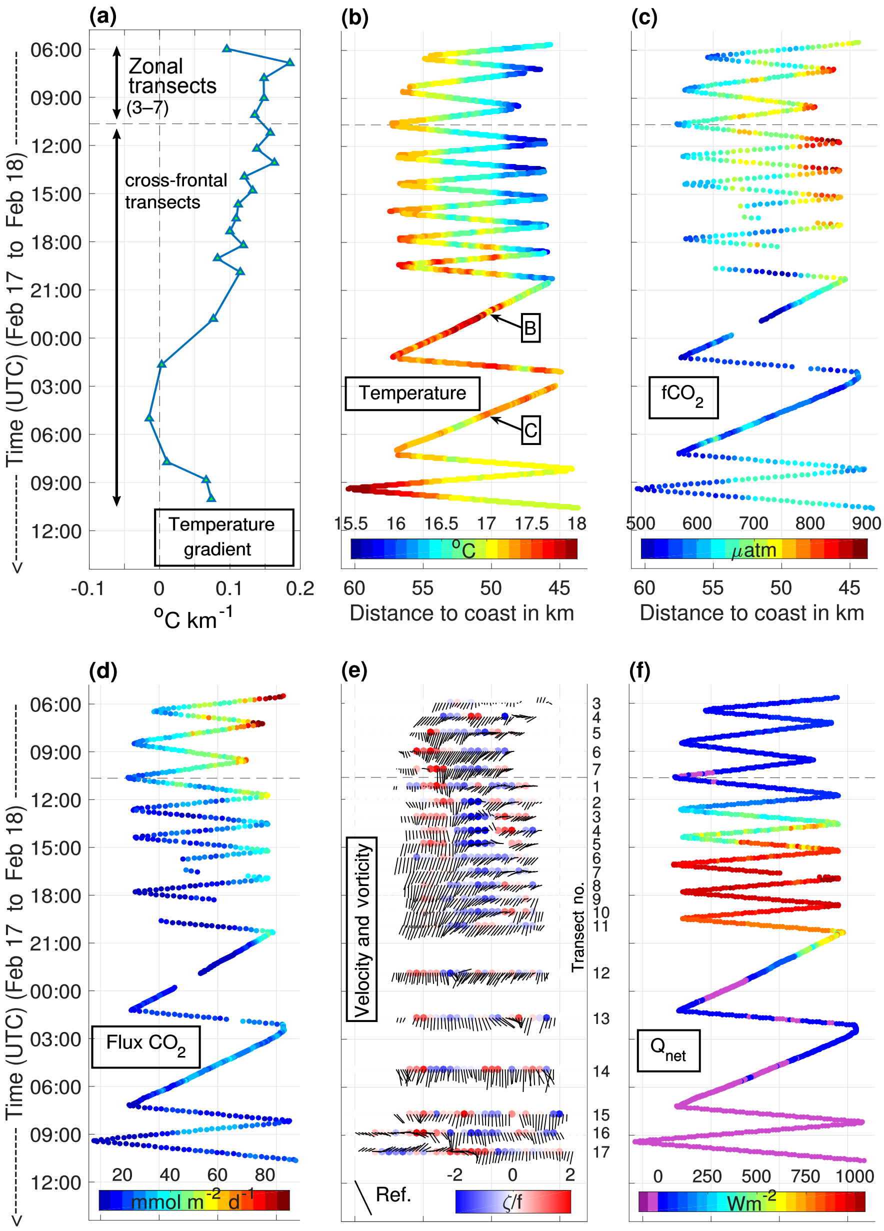

Figure 6. Hovmöller diagrams of the cross-frontal surface temperature gradient **(a)**, underway surface temperatures **(b)**, surface fCO_2 **(c)**, ocean–atmosphere CO_2 fluxes **(d)**, mean current velocities in the upper 40 m (black lines) and vorticity (colored circles) **(e)**, and diabatic surface heating **(f)** for the last 5 zonal transects and the subsequent 17 cross-frontal transects. The horizontal dashed line indicates the transition from zonal transects to repeated cross-frontal transects. Temperature gradients in **(a)** are calculated using a linear fit to the surface temperature transect shown in **(b)**. In **(b)** the position of transects B and C is indicated. The vorticity of the vertically averaged velocity in **(e)** is calculated as $\zeta = \partial u_{\mathrm{al}}/\partial y$ (Rudnick, 2001), where u_{al} is the along-front velocity and y is the cross-frontal distance, taken to be 2 km, comparable to the mixed-layer deformation radius. The reference arrow in the bottom left corner anchored at 60 km from the coast indicates a flow with 0.3 m s^{-1} in the onshore (cross-front) and 0.3 m s^{-1} in the poleward along-front direction. The vorticity is normalized by the Coriolis parameter to give a proxy for the Rossby number. Velocity and vorticity are plotted at the mean time for each transect. Time is given in UTC.

ity of 35.1, yielding an uncertainty of density in the range of $0.1\,\mathrm{kg\,m^{-3}}$ and in vertical buoyancy fluxes of 1 %. The mean values of $\langle w'b' \rangle_{Q_{\mathrm{net}}}$ for each transect are shown in Fig. 9. During both night and daytime, the surface layer gains buoyancy. In the night this vertical buoyancy flux is weak, with a rate of less than $1 \times 10^{-8}\,\mathrm{m^2\,s^{-3}}$. During the day, vertical buoyancy fluxes of more than $5 \times 10^{-7}\,\mathrm{m^2\,s^{-3}}$ act to stratify the surface layers.

While surface heat fluxes are shown to contribute to the overall evolution of the temperature field, they cannot explain the across-frontal variability. In particular, the observed temperature changes below the surface layer seem to be unconnected to surface heating. Thus, dynamical processes are investigated in the following to understand the reduction of the cross-frontal temperature gradient.

4.2 Ekman transport

Throughout the experiment the wind speed changed significantly from almost 12 to $4\,\mathrm{m\,s^{-1}}$, while the wind direction stayed almost parallel to the front in the same direction as the frontal jet, i.e., down-frontal (Fig. 4). The cross-frontal Ekman velocity is calculated as $u_{\mathrm{Ek}} = \tau_0/(f \rho_0 H_{\mathrm{ML}})$, where $\tau_0 = \rho_{\mathrm{air}} \left(c_{\mathrm{d}} u_{10}^2\right)$ is the neutral along-frontal surface wind stress. The drag coefficient c_{d} and the along-frontal wind speed at 10 m height u_{10} are calculated following Smith (1988). The mean density within the Ekman layer ρ_0 is approximated by the surface density ρ. Assuming a mixed-layer depth $\mathrm{H_{ML}} = 10\,\mathrm{m}$, Ekman current velocities reach up to $0.5\,\mathrm{m\,s^{-1}}$ and are always directed offshore (figure not shown). During the period of the developing surface temperature anomalies, the Ekman velocity drops to $\sim 0.1\,\mathrm{m\,s^{-1}}$, agreeing with the observed cross-front velocities close to the surface (Fig. 7a, c). The large uncertainties in surface salinity lead to only minor errors in Ekman velocity of less than $10^{-3}\,\mathrm{m\,s^{-1}}$. The choice of the mixed-layer depth has a far larger impact due to the inverse proportionality. For example choosing $H_{\mathrm{ML}} = 5\,\mathrm{m}$ leads to Ekman velocities larger by a factor of 2. The clear offshore direction of the Ekman transport is not affected by these uncertainties.

The wind-driven Ekman transport is associated with a non-geostrophic overturning circulation in the vertical/cross-frontal plane (Thomas et al., 2008). For such an overturning circulation it is possible to infer the associated vertical buoyancy flux $\langle w'b' \rangle$. The Ekman buoyancy flux (EBF) is given by $\langle w'b' \rangle_{\mathrm{EBF}} = \tau_0 \cdot \nabla b/(\rho_0 f)$ (Thomas and Lee, 2005), where f is the Coriolis parameter. ∇b is the cross-frontal buoyancy gradient, taken as the slope from a linear fit to the surface buoyancy across the front. Buoyancy is calculated as $b = -g(\rho - \rho_{\mathrm{r}})/\rho_{\mathrm{r}}$ using a reference density $\rho_{\mathrm{r}} = 1035\,\mathrm{kg\,m^{-3}}$.

Calculating the buoyancy gradient with a constant salinity value of $35.1\,\mathrm{g\,kg^{-1}}$ is likely to yield an error for the Ekman buoyancy fluxes as the initial CTD transect indicates a cross-fontal surface salinity gradient of $-5 \times 10^{-3}\,\mathrm{g\,kg^{-1}\,km^{-1}}$. Hence, this salinity gradient is imposed onto the mean value of $35.1\,\mathrm{g\,kg^{-1}}$ to estimate the cross-frontal buoyancy gradient. Figure 9 shows the buoyancy fluxes calculated for each transect. The EBF is enclosed by an uncertainty range related to the surface salinity gradient. The edges of this uncertainty range stem from the cases of no cross-frontal salinity gradient and double the initially observed cross-frontal gradient.

The down-frontal wind drives continuous Ekman transport from the cold to the warm side of the front, thus acting to keep the isopycnals strongly tilted, rather than directly transporting warm water onshore. Correspondingly, the EBF is predominantly negative, signifying a destratification within the surface layer, inhibiting the slumping of isopycnals. During the cross-frontal transects, the EBF weakens drastically from -1×10^{-6} to $-2 \times 10^{-7}\,\mathrm{m^2\,s^{-3}}$. Only during cross-frontal transects 13–15 do the buoyancy fluxes change sign, which goes along with the turnaround of the surface temperature gradient (Fig. 6a) while the Ekman velocity continues to be directed offshore. Afterwards, during the reformation of the front towards the end of the experiment on 18 February, the EBF returns to negative values.

The results above show that the weakening of the temperature front is not directly caused by onshore Ekman transport. Still, the reduction in down-frontal (equatorward) wind speed and the associated weakening in offshore Ekman transport can change the frontal stability. During most of the experiment's duration, the EBF inhibited a slumping of isopycnals. However, this flux weakened over the course of the experiment, potentially allowing other processes such as surface heat fluxes or mixed-layer instabilities to become more important.

4.3 Mixed-layer instabilities (MLIs)

Baroclinic instabilities confined to the mixed layer are referred to as submesoscale mixed-layer instabilities (MLIs; Haine and Marshall, 1998; Boccaletti et al., 2007). They act to restratify the mixed layer by extracting potential energy from horizontal density gradients within the vertically well-mixed surface layer and convert this into eddy kinetic energy, through formation of mixed-layer eddies which accomplish the cross-frontal transport and exchange. With their short timescales of $\mathcal{O}(f^{-1})$, submesoscale MLIs are thought to be efficient in converting lateral density fronts to a stratified mixed layer. Their horizontal scales are given by $L = N H_{\mathrm{ML}}/f$, where $N = \sqrt{g/\rho\,(\partial \rho/\partial z)}$ is the small but non-vanishing stratification within the mixed layer (Thomas et al., 2008). Based on the initial CTD transect A (shown in Fig. 5) this length scale L is calculated to be $2.5 \pm 1.5\,\mathrm{km}$. The large error accounts for the uncertainties in the mean mixed-layer stratification, which is estimated to be $N \approx (6 \pm 4) \times 10^{-3}\,\mathrm{s^{-1}}$. The inverse of the growth rate of MLI $(2\pi/f)$ can be used as the associated timescale, which amounts to ~ 2.1 days in the present case. The proximity of the study region to the equator associated with relatively long inertial

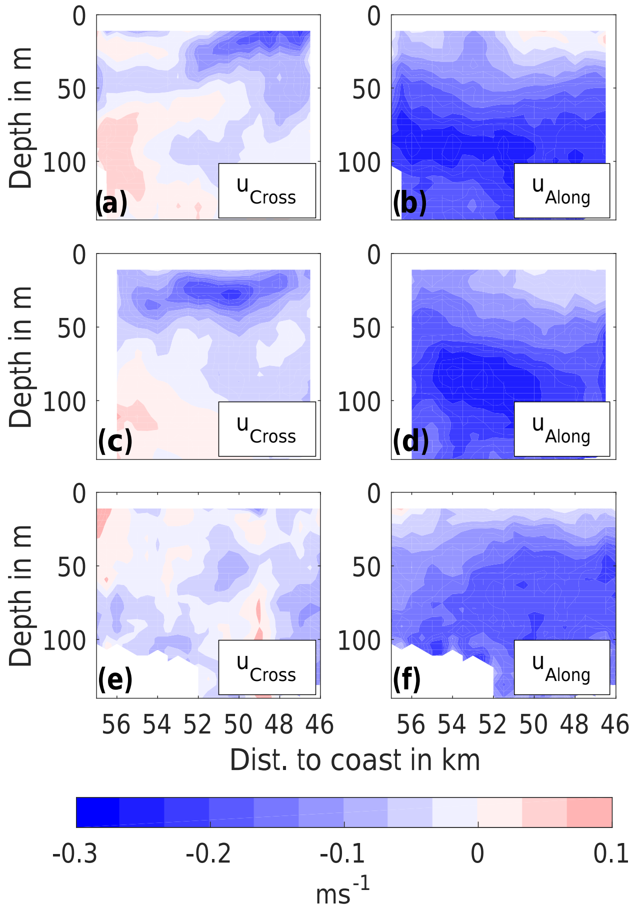

Figure 7. Mean cross- and along-front current velocities for cross-frontal transects 1–6 in **(a)** and **(b)**, 7–11 in **(c)** and **(d)**, and 12–17 in **(e)** and **(f)**. Currents are horizontally binned onto a 500 m grid and subsequently averaged.

timescales makes it possible to capture well the variability by means of underway measurements.

Repeated observations of coherent surface temperature anomalies and their intensification between 15:00 and 20:00 on 17 February around 50 km away from the coast might indicate the development of MLI (Fig. 6b). Preceding their appearance are small anomalies in the current field averaged over the upper 40 m (Fig. 6e). There, the mostly southbound flow reverses and flows weakly northward, producing large relative vorticity values (cross-frontal transects 3, 4, 5). This points towards eddying structures which could be associated with MLI. The mixed-layer depth, estimated by a $\Delta T = 0.2\,°\mathrm{C}$ criterion, shows a shallowing throughout the experiment. While the average mixed-layer depth is 15 m during the CTD transect A, it reduces to 3 and 5 m during transects B and C, respectively. We applied linear stability analysis, which provides vertical modes of the growth of baroclinic instabilities (Brüggemann and Eden, 2014; Thomsen et al., 2014), to the laterally averaged stratification and geostrophic current shear profile from the initial CTD section (Fig. 10b, c). This analysis reveals the existence of both a deep mesoscale mode and a shallow mode, confined to the mixed layer (Fig. 10a, d, e). The horizontal length scale of the deep mode is about 200 km, while it is only 8.7 km for the shallow mode. This length scale is of the same order of magnitude as the expected mixed-layer deformation radius L and the size of the observed surface temperature anomalies. The initial growth rate of the shallow mode calculated from linear stability analysis is 0.5 day^{-1}. Once the instabilities grow too large, nonlinearities dominate the instability process and linear stability analysis may not provide a useful description of the evolution of the instabilities (Thomsen et al., 2014). However, the calculated growth rate is relatively slow compared to the observed rapid decline of the cross-frontal temperature gradient. Also, the inferred shallow mode is limited to ~ 15 m depth, i.e., the mixed layer (Fig. 10e). Thus, instability-induced changes of the velocity field at 30 m depth would require an interaction with the deep mode (Fig. 10d).

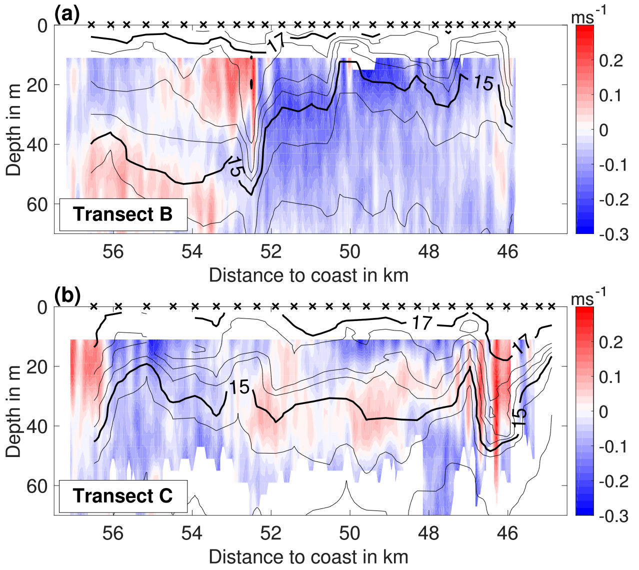

Figure 8. Temperature (black contour lines) and cross-front velocity (color-coded) for Transects B **(a)** and C **(b)** conducted as the 12th and 14th cross-frontal transect, starting on 17 February 21:00 and 18 February 03:00, respectively. Black crosses show the location of the temperature profiles from the microstructure probe. For both transects the ship moved away from the coast (right to left).

Similar to Ekman dynamics, a secondary overturning circulation is driven by MLI. It is important to note that while an EBF is associated with strong diapycnal mixing, pure mixed-layer instabilities are of an adiabatic nature. According to Fox-Kemper et al. (2008) the vertical buoyancy flux due to MLI given by $\langle w'b' \rangle_{\mathrm{MLI}} = C H_{\mathrm{ML}}^2 (\nabla b)^2 / |f|$ (where $C = 0.08$ is a constant) always tends to reduce the lateral bouyancy gradient. Throughout the experiment the $\langle w'b' \rangle_{\mathrm{MLI}}$ values are positive, indicating a restratification of the mixed layer. However, the buoyancy flux associated with MLI is in

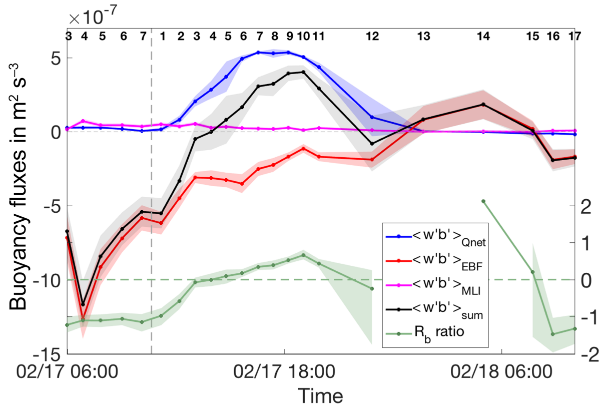

Figure 9. Vertical buoyancy fluxes associated with surface heating (blue), Ekman transport (red), and mixed-layer instabilities (magenta). The shaded areas around the Ekman buoyancy flux (EBF) and the buoyancy flux associated with mixed-layer instabilities (MLI) account for uncertainties in the surface salinity gradient (see text for more details). The shaded uncertainty range for vertical buoyancy fluxes due to surface heating is given as 1 standard deviation obtained from sectional averaging. The sum of the three processes is given by the black line. The uncertainty is given as the maximum error resulting from the three processes. The R_b ratio (green) and its uncertainty are treated similarly. For cross-frontal transect 13 and 14 no R_b value or error can be stated due to the vanishing denominator in the definition of R_b. $\log_{10}(R_\mathrm{b}) > 0$ points towards a net restratification, while $\log_{10}(R_\mathrm{b}) < 0$ indicates a destabilization of the water column. For calculation details of all quantities see text. Time is given in UTC. The small black numbers on top indicate the respective zonal or cross-frontal transect number.

general about 10 times smaller than the EBF. During the stable front the buoyancy flux associated with MLI $\langle w'b'\rangle_\mathrm{MLI}$ is less than $1\times10^{-7}\,\mathrm{m}^2\,\mathrm{s}^{-3}$ and reduces afterwards. Calculations are done with $H_\mathrm{ML} = 15$ m based on the CTD transect. This is likely to be an upper bound for the mixed-layer depth during the main experiment, as transects B and C show a much shallower mixed layer. Both linear stability analysis and buoyancy flux estimates imply that MLIs are present, acting to restratify the mixed layer, but seem to be too slow and too confined to the surface layer, such that observed changes at depth cannot be explained by MLIs alone.

4.4 Surface gravity current

In the presence of lateral density gradients, an unforced surface mixed layer is subject to pressure-driven gravity currents, where lighter water spreads on top of the denser waters on timescales below the inertial period, i.e., independent of rotational effects (e.g., Kao et al., 1977). The observed decrease in down-frontal wind speed could therefore give rise to the spreading of a buoyant plume down the temperature gradient. The rapid decline and even a slight reversal of the temperature front is captured well by transects B and C (Fig. 8). Within 6 h the structure of both the temperature and cross-frontal velocity fields changed significantly. While transect B still shows a pronounced (subsurface) frontal signature, the isotherms in transect C are close to horizontal. The temperature field in transect C is subject to distortion through internal waves. At km 46, the undulating isotherms go along with an oscillating signal in cross-front velocity, agreeing with internal waves propagating up the continental shelf. The strong depression of isotherms at km 57 could be the onset of another internal wave signal. In transect B, the temperature and velocity field exhibit a strong anomaly at km 52.5. There, a narrow but strong depression of the temperature field coincides with a region of strong convergence in the cross-frontal direction. Unlike in transect C, the attribution of the depression of the isotherms to an internal wave signal is not straightforward as the velocity field does not

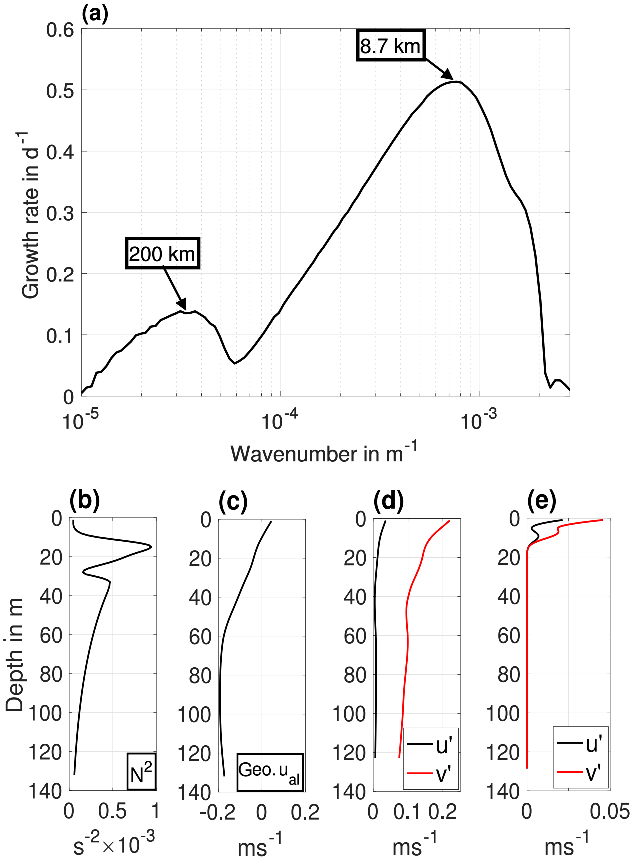

Figure 10. (a) Initial growth rate of baroclinic instabilities obtained from linear stability analysis, applied to the frontal state during the CTD section (transect A). The local maxima of the growth rate are labeled by their corresponding length scale in kilometers. The smoothed stratification and geostrophic along-frontal velocity profiles used as the background state are shown in panels **(b)** and **(c)**. A deep mode at large horizontal scales (200 km) and a shallow mode, associated with mixed-layer instabilities and short horizontal length scales (8.7 km), are present. The corresponding anomalies for the cross-front (u) and along-front (v) velocities are shown in panels **(d)** and **(e)** for the deep and shallow modes, respectively.

show an oscillating behavior in the vicinity of the depression. This might be attributed to aliasing of the signal due to too few hydrographic observations, which do not capture the short period of the internal waves.

Any density (here temperature) front is associated with a cross-frontal pressure gradient. In coastal upwelling regimes, this pressure gradient is largely in geostrophic balance manifesting itself in an along-frontal jet. However, if the wind field setting up the frontal system becomes too weak, the tilted isopycnals might start to slump, with the light surface waters offshore pushing over the denser surface water located further onshore. Thus, baroclinic temperature fronts can be eroded by gravity currents flowing down the pressure gradient across the front. Observations from river plumes show that the head of a gravity current may excite large-amplitude internal waves (Nash and Moum, 2005). These are either arrested at the leading edge of the gravity current or may propagate ahead of it if the current's advection speed is lower than that of the wave propagation speed. Assuming that the anomaly signals in transect B (at km 52.5) and C (at km 46) belong to the same internal wave package that propagates at the leading edge of the gravity current, a propagation speed of $0.4\,\mathrm{m\,s^{-1}}$ is estimated using a time difference of 4.5 h and a distance of 6.5 km. In a simple two-layer model, the propagation speed of the gravity current in deep ambient fluid is given by $c = \sqrt{g'H}$, where $g' = g\Delta\rho/\rho$ is the reduced gravity, $\Delta\rho$ is the density difference between the two layers, and H is the thickness of the upper layer (Shin et al., 2004; Dale et al., 2008). Assuming a two-layer problem in the observed frontal setup with $H = 30\,\mathrm{m}$ as the average depth of the 15 °C isotherm, $g' = 5 \times 10^{-3}\,\mathrm{m\,s^{-2}}$ derived from densities calculated at 10 and 50 m depth, and assuming a salinity of 35, the theoretical propagation speed c can be estimated to be $0.4\,\mathrm{m\,s^{-1}}$, thus agreeing with the observed propagation speed. If the temperature anomalies in sections B and C represent an internal wave package propagating at the leading edge of a gravity current, the internal wave propagation speed estimates above suggest that a density-driven gravity current is a possible mechanism behind the abrupt degradation of the temperature front. In contrast to the other analyzed processes it is capable of explaining subsurface changes in the temperature field.

5 Comparison of buoyancy fluxes

Over the whole experiment, three of the four analyzed physical processes are comparable in terms of the associated vertical buoyancy fluxes (Fig. 9). The ratio

$$R_\mathrm{b} = \frac{\langle w'b'\rangle_{Q_\mathrm{net}>0} + \langle w'b'\rangle_\mathrm{MLI} + \langle w'b'\rangle_{\mathrm{EBF}>0}}{\langle w'b'\rangle_{Q_\mathrm{net}<0} + \langle w'b'\rangle_{\mathrm{EBF}<0}} \tag{1}$$

allows for a statement on the combined effect of the Ekman buoyancy flux, surface heating, and MLI (Mahadevan et al., 2010; Taylor and Ferrari, 2011). The numerator only contains terms associated with stratification, i.e., positive buoyancy fluxes. For example the buoyancy flux associated with MLIs is always positive and thus appears only in the numerator. The EBF, however, changes sign during the experiment. During the parts of the experiment with positive EBF it will contribute to the term $\langle w'b'\rangle_{\mathrm{EBF}>0}$ in the numerator. If the EBF is negative, its modulus will appear in the denominator as $\langle w'b'\rangle_{\mathrm{EBF}<0}$. The same applies to the surface heating buoyancy fluxes. As a result, if $R_\mathrm{b} > 1$, the mixed layer is subject to restratification associated with a slumping of isopycnals, whereas $R_\mathrm{b} < 1$ implies a destratification, i.e., mixing in the surface layer. During the time of the development of the coherent surface temperature anomalies (cross-frontal transects 7–11), the combination of the three processes favor a restratification of the mixed layer (Fig. 9). Linear stability analysis confirms the existence of a shallow baroclinic mode, which shows growth rates of 0.5 $\mathrm{day^{-1}}$ on length scales of 8.7 km. The latter agrees well with the extent of the observed temperature anomalies and the mixed-layer radius of deformation calculated from the initial CTD transect. While the temporal scale of the shallow mode is in agreement with the development of the surface temperature anomalies, its impact in the rapid decline of the temperature front around 00:00 on 18 February is probably low, as the growth rate at the initial phase of the instability seems too small. Furthermore, the low associated buoyancy fluxes (Fig. 9) indicate that MLI may contribute only to a small degree to the observed change in the temperature gradient across the front.

In contrast, the buoyancy fluxes associated with surface heating and cross-frontal Ekman transport (Fig. 9) contribute to the changes in sign of the sum of the buoyancy flux (and to $R_\mathrm{b} > 1$) during 17 February. Even though the strength of the diabatic heating agrees well with the amplitude of the developing surface temperature anomaly, stronger-than-observed horizontal gradients in surface heating are required to induce the observed lateral differences in warming. Furthermore, the nature of this buoyancy flux is purely vertical and thus unable to create horizontal gradients in the case of spatially uniform heating, opposed to buoyancy fluxes associated with MLI or Ekman dynamics, which are fully three-dimensional.

The buoyancy flux related to a gravity current is mainly lateral. However, if the warm water spreads on top of the cold water on the onshore side of the front, a vertical buoyancy flux is induced. In a closed domain the mean vertical buoyancy flux can be estimated following $\partial E_\mathrm{p}/\partial t \approx -\langle wb\rangle$ (Peltier and Caulfield, 2003; White and Helfrich, 2013), thus by comparing volume-averaged potential energies E_p at two different points in time t. In a two-dimensional domain the volume-averaged potential energy is calculated as $E_\mathrm{p} = (hd)^{-1}\int_d\int_0^h bz\,\mathrm{d}z\,\mathrm{d}x$, where d is the lateral distance and h is depth. Using a constant salinity value of 35 the buoyancy field is calculated for transects B and C. Considering the upper 70 m on the initially cold side of the front (i.e., only east of 52 km offshore) a vertical buoyancy flux of $2.7 \times 10^{-6}\,\mathrm{m^2\,s^{-3}}$ is estimated. Laterally extending the domain to the full transects B and C reduces the vertical buoyancy flux to $1.8 \times 10^{-6}\,m^2\,s^{-3}$. As the transects B and C have no closed boundaries, the estimates carry large uncertainties. The pressure-driven gravity current is, however, assumed to be fully captured by both transects so that its associated effect should be captured. In the context of a closed domain the subsurface temperature reduction on the initially warm side of the front could be associated with an upward suction of colder water balancing the downward pumping of surface water on the cold side of the front (Fig. 8).

The estimated flux due to the gravity current is much larger than the buoyancy fluxes associated with the other processes described above during the cross-frontal transects 12–14, regardless of the chosen cross-frontal width considered. Only the EBF during the beginning of the experiment is of the same order of magnitude.

6 Discussion

Gathering data from multiple ship surveys, Friederich et al. (2008) observed oceanic outgassing of CO_2 in the Peruvian upwelling region throughout the year. On average the authors estimated a sea-to-air CO_2 flux of $5\,mol\,m^{-2}\,yr^{-1}$. On seasonal timescales, the flux varied between 2.5 and $10\,mol\,m^{-2}\,yr^{-1}$ associated with weak and strong upwelling periods, respectively. Although Friederich et al. (2008) focused on the large-scale distribution of surface CO_2 fluxes and the associated mechanisms, they further detected strong variability of CO_2 fluxes on short time and space scales ($\mathcal{O}$(hours–days) and $\mathcal{O}$(km)), which contributes significantly to the overall CO_2 budget.

Motivated by their findings, the study presented here focuses on the pronounced submesoscale variability of surface CO_2 in the Peruvian upwelling region at 13.7° S. Our observations show CO_2 outgassing rates between 3.5 and $30\,mol\,m^{-2}\,yr^{-1}$ which are in line with the outgassing signals observed by Friederich et al. (2008), even after accounting for the difference in converting our values from partial pressures to fugacities (difference usually about 3 %). Our peak sea–air fluxes reaching up to $80\,mmol\,m^{-2}\,day^{-1}$ are distinctly higher than the maximum flux of $12.4\,mmol\,m^{-2}\,day^{-1}$ reported by Friederich et al. (2008) for a measurement campaign in the month of February. At the same time, our peak flux is only slightly higher than maximum flux values reported from other months. The results from Friederich et al. (2008) were re-scaled to a much larger area (5–15° S), have been subject of spatial extrapolation and smoothing, and were calculated with the sea–air gas exchange parameterization by Wanninkhof (1992), which tends to overestimate the gas transfer velocities (see Wanninkhof, 2014). Simply using the Wanninkhof (1992) parameterization instead of the Nightingale et al. (2000) parameterization yields 17 % higher fluxes, already indicating that it is difficult to draw a direct comparison between both data sets. Nonetheless, both studies agree in that the near-coastal zone off Peru acts as a rather strong source of CO_2 to the atmosphere, and from our data it seems clear that the onshore side of the upwelling front could be associated with an important enhancement of CO_2 outgassing. The conditions observed in this study are not necessarily representative for February conditions. Many processes on different timescales can alter the upwelling frontal structure and intensity off Peru, for instance the state of the El Niño–Southern Oscillation (Espinoza-Morriberón et al., 2017) or coastally trapped waves propagating along the Peruvian coast (Pietri et al., 2014). The aim of this study is rather to analyze a suite of processes involved in the evolution of the upwelling front and surface fCO_2 on short space and timescales ($\mathcal{O}$(1 km), $\mathcal{O}$(0.5 day)).

The down-frontal wind is an important ingredient in maintaining tilted isopycnals in the surface layer. The EBF dominates all other buoyancy fluxes during the strong wind period (Fig. 9). In a study by Dale et al. (2008), a restratification of the mixed layer is observed in connection with a frontal decay in the upwelling system off Oregon on length scales comparable to those presented here. In their study, a reversal of the wind direction plays a crucial role in driving the frontal decay by inducing an Ekman transport down the cross-frontal pressure gradient. For the frontal decay presented here, the wind is always directed down-frontal and does not change significantly. The cross-frontal wind component is weak (mostly less than $3\,m\,s^{-1}$) and alternates in direction between onshore and offshore without any clear dominance (Fig. 4). As a result, Ekman transport and the associated buoyancy flux do not change direction. Still, the strong reduction in cross-frontal Ekman transport could potentially give way for other mechanisms.

Pronounced changes across the front are shown to occur in two steps after the distinct reduction in down-frontal wind speed with a time lag of about 9 h. The first step is characterized by the gradual development and strengthening of coherent surface temperature anomalies, while the second is characterized by a sudden decline and even slight reversal of the temperature gradient. Transects B and C (Fig. 8) show that changes in the temperature field are thereby not limited to the surface layer, but reach down to 50 m. To identify the underlying processes, the frontal evolution is described above in a two-dimensional framework, i.e., in the vertical/cross-frontal plane. The variability induced by along-frontal advection is neglected. This assumption seems valid, as the along-frontal current velocities reduce close to zero in proximity to the surface (Fig. 7b, d, e). Furthermore, the fact that the cross-frontal transects show coherent signals, even though not all cross-frontal transects were performed on the exact same track but about 1 km apart, points towards a weak along-frontal flow variability. Still, the two-dimensional framework allows for various hypotheses about the driving mechanisms behind the observed changes.

The analyses have shown that the diurnal surface heating is able to explain the majority of the mean increase in surface temperatures. During the phase of maximum heating the associated positive buoyancy flux into the ocean outweighs the permanent reduction in surface buoyancy by the down-frontal wind stress (Fig. 9). However, the spatially homogeneous heating is unable to account for the developing small-scale temperatures anomalies. As a result, submesoscale MLI have been investigated as they are shown to restratify the surface mixed layer and are thereby capable of generating lateral gradients and anomalies. Linear stability analysis indeed shows the presence of a shallow baroclinic mode confined to the mixed layer (Fig. 10). While the length scale of this mode roughly meets the observed horizontal extent of the temperature anomalies and the mixed-layer deformation radius, the instability seems to grow too slowly to be the dominant dynamical process involved in the frontal decay. Hence additionally, the vertical buoyancy fluxes associated with MLI are an order of magnitude smaller than those related to surface heating or Ekman dynamics (Fig. 9).

The low-latitude location of the experiment site at 13.77° S results in a rather long inertial time period of $T_{in} = 2\pi/f = 2.1$ days. Thus, the sudden changes observed from hydrographic sections B and C within a time span of 6 h suggest that processes influenced by Earth's rotation are potentially less important in the final weakening of the temperature front. Propagating buoyant plumes related to river discharge (Nash and Moum, 2005) or frontal zones in upwelling regimes (Walter et al., 2016) are common dynamical processes in continental shelf regions. In fact, Dale et al. (2008) also identified such a pressure-driven gravity current propagating across the front, once the wind forcing had changed. For our case, using a limited amount of hydrographic information, a propagation speed of $0.4\,\mathrm{m\,s^{-1}}$ can be identified. This proves to match well with the theoretical estimate for a two-layer system. The present stratification, however, complicates the distinction of a sharp density gradient to apply the gravity current theory. Furthermore, stratified ambient water decreases the propagation speed of a gravity current compared to the two-layer system (Ungarish and Huppert, 2002). Still, hinting towards the observation of a gravity current, both transect B and C exhibit strong internal wave signals, which have been observed at the leading edge of such buoyant plumes (Nash and Moum, 2005; Bourgault et al., 2016). Of all mechanisms presented, the gravity current is the only one that may account for the fast changes up to 50 m depth. In contrast, the stability analysis suggests that MLIs are mainly active in the mixed layer and could only effect lower layers by interacting with the deep mode (Ramachandran et al., 2014; Capet et al., 2016).

In this study we set focus solely on the role of physical processes driving the small-scale distribution of $f\mathrm{CO_2}$. We argue that the timescales considered here are too short to allow for significant contributions of biological processes in driving $f\mathrm{CO_2}$ changes across the front. The strong correlation of surface temperature and $f\mathrm{CO_2}$ imply that the $f\mathrm{CO_2}$ variability is dominated by two processes: firstly, the temperature dependent solubility of gases in seawater and secondly, warm offshore surface water pushing on top of CO_2-enriched upwelled water, thus creating a mechanical barrier for air–sea gas exchange. However, the weakening of the correlation over time (Fig. 3) indicates that other processes, such as biological activity, might become increasingly important. A more thorough analysis from a biogeochemical perspective incorporating these effects is needed (Mahadevan et al., 2004). Consistently, physical processes seem to be able to account for the small-scale variability observed by Friederich et al. (2008), and understanding them could be crucial to establish a reliable CO_2 budget for the Peruvian upwelling region. Likewise, it is mandatory to have accurate observations of the near-shore wind field, as it proved to be an important factor contributing to the small-scale evolution of the upwelling front. Modern satellite wind products are still too coarse to resolve the submesoscale frontal variability or other small-scale variations such as land–sea breezes or an enhanced near-shore wind stress curl. They are thus not fully reliable within 25 to 50 km from shore (Croquette et al., 2007; Albert et al., 2010).

7 Conclusions

High-resolution underway measurements are a useful tool in observing submesoscale variability on scales of $\mathcal{O}(1)$ km. Pronounced changes in the $f\mathrm{CO_2}$ and temperature fields were observed across an upwelling front within hours, providing evidence of high short-term variability in the sea–air CO_2 exchange off Peru. We provide evidence of the complex submesoscale distribution of surface CO_2 in the Peruvian upwelling system and its tight connection to the strong variability in surface temperature. It thus appears that on these timescales the evolving $f\mathrm{CO_2}$ distribution is controlled by physical processes.

Outgassing of CO_2 dropped from 80 to less than $10\,\mathrm{mmol\,m^{-2}\,day^{-1}}$ within less than 24 h. We showed that this drastic change can be explained by physical processes associated with a weakening of the cross-frontal temperature gradient following a significant decrease in down-frontal (equatorward) wind speed. The initially geostrophically balanced front with a length scale of 10 km vanished within few hours, thereby removing a surface temperature difference of 1 °C over 10 km. Hydrographic data shows pronounced changes in the temperature field at depths of up to 50 m. Despite the lack of direct onshore transport of warm water by Ekman dynamics, the wind played a major role in maintaining the front in the beginning of the experiment. The decay of the down-frontal wind gave rise to the development of submesoscale mixed-layer instabilities and potentially allowed for a gravity current to propagate down the cross-frontal pressure gradient. The mixed-layer instabilities, however, appear to be too shallow and too slow to be able to account for the complete removal of the cross-frontal temperature gradient. However, the onset of a surface gravity current would be consistent with the observed changes in the subinertial period. In addition, our analysis shows that multiple processes act simultaneously and are likely to interact, thus complicating the identification of a single dominant mechanism responsible for the fast observed changes in surface $f\mathrm{CO}_2$.

At present, a low CO_2 data coverage within the Peruvian upwelling region (e.g., in SOCAT; Bakker et al., 2016) complicates the establishment of a reliable climatology, as done by Takahashi et al. (2014) or more recently Landschützer et al. (2017). From our study the importance of the wind and temperature variability on timescales of $\mathcal{O}$(hours) in setting the strength of sea–air CO_2 fluxes becomes obvious. When coupled with CO_2 measurements the use of sea surface temperature and wind products, which capture the high temporal and spatial variability, could lead to improved future estimates of a CO_2 flux climatology off Peru. In order to understand the large-scale impact of short-term variability of an upwelling ecosystem, one way forward would be the establishment of multi-platform observation networks in which continuous in situ data are complemented by satellite observations and measurements from autonomous platforms (e.g., gliders, as those conducted by Ohman et al. (2013) in the California Current System. A further example is the moored CO_2 observations from Lefèvre et al. (2008) and Lefèvre and Merlivat (2012) which help to constrain regional budgets and variability of CO_2 for the eastern tropical Atlantic and could also be used to reliably estimate the net carbon community production in this area.

Data availability. The large-scale sea surface temperature (SST) data were retrieved from NASA's OceanColor project as daily satellite MODIS Aqua and Terra SST data (https://oceancolor.gsfc.nasa.gov/). The large-scale wind field Advanced Scatterometer (ASCAT) wind data (Bentamy and Fillon, 2012) were taken from the Asia-Pacific Data-Research Center at the University of Hawai'i (http://apdrc.soest.hawaii.edu/datadoc/ascat.php).

According to the SFB 754 data policy (https://www.sfb754.de/de/data), all data associated with this publication are accessible upon publication under https://doi.org/10.1594/PANGAEA.881049 (Köhn et al., 2017).

Author contributions. EEK performed the analysis and wrote the manuscript. ST designed the experiment and contributed to the manuscript. DLA-M measured and provided the CO_2 data and contributed to the manuscript. TK was chief scientist on M93, stimulated the analysis, and gave scientific guidance. All authors reviewed and commented on the manuscript.

Competing interests. The authors declare that they have no conflict of interest.

Acknowledgements. This work is a contribution of Sonderforschungsbereich 754 Climate-Biogeochemistry Interactions in the Tropical Ocean (www.sfb754.de), which is funded by the Deutsche Forschungsgemeinschaft (DFG). We are grateful to the Peruvian authorities for the permission to carry out scientific work in their national waters. Special thanks go to the captain and the crew of the R/V *Meteor* for their support during the M93 cruise. We are grateful to Tobias Steinhoff for making available the CO_2 sensor as well for his technical support during the cruise. We further thank Liam Brannigan, Leah Johnson, Karl Bumke, and the meteorologists of the DWD for helpful discussions of the results. Damian L. Arévalo-Martínez received additional funding support through the BMBF funded SOPRAN II (FKZ 03F0611A) project, as well as the Future Ocean Excellence Cluster at Kiel University (CP0910), and the EU FP7 project InGOS (grant agreement 284274).

The article processing charges for this open-access
publication were covered by a Research
Centre of the Helmholtz Association.

Edited by: Piers Chapman
Reviewed by: two anonymous referees

References

Albert, A., Echevin, V., Lévy, M., and Aumont, O.: Impact of nearshore wind stress curl on coastal circulation and primary productivity in the Peru upwelling system, J. Geophys. Res.-Oceans, 115, C12033, https://doi.org/10.1029/2010JC006569, 2010.

Arévalo-Martínez, D. L., Beyer, M., Krumbholz, M., Piller, I., Kock, A., Steinhoff, T., Körtzinger, A., and Bange, H. W.: A new method for continuous measurements of oceanic and atmospheric N_2O, CO and CO_2: performance of off-axis integrated cavity output spectroscopy (OA-ICOS) coupled to non-dispersive infrared detection (NDIR), Ocean Sci., 9, 1071–1087, https://doi.org/10.5194/os-9-1071-2013, 2013.

Arévalo-Martínez, D. L., Kock, A., Löscher, C. R., Schmitz, R. A., and Bange, H. W.: Massive nitrous oxide emissions from the tropical South Pacific Ocean, Nat. Geosci., 8, 530–533, https://doi.org/10.1038/ngeo2469, 2015.

Bakker, D. C. E., Pfeil, B., Landa, C. S., Metzl, N., O'Brien, K. M., Olsen, A., Smith, K., Cosca, C., Harasawa, S., Jones, S. D., Nakaoka, S.-I., Nojiri, Y., Schuster, U., Steinhoff, T., Sweeney, C., Takahashi, T., Tilbrook, B., Wada, C., Wanninkhof, R., Alin, S. R., Balestrini, C. F., Barbero, L., Bates, N. R., Bianchi, A. A., Bonou, F., Boutin, J., Bozec, Y., Burger, E. F., Cai, W.-J., Castle, R. D., Chen, L., Chierici, M., Currie, K., Evans, W., Featherstone, C., Feely, R. A., Fransson, A., Goyet, C., Greenwood, N., Gregor, L., Hankin, S., Hardman-Mountford, N. J., Harlay, J., Hauck, J., Hoppema, M., Humphreys, M. P., Hunt, C. W., Huss, B., Ibánhez, J. S. P., Johannessen, T., Keeling, R., Kitidis, V., Körtzinger, A., Kozyr, A., Krasakopoulou, E., Kuwata, A., Landschützer, P., Lauvset, S. K., Lefèvre, N., Lo Monaco, C., Manke, A., Mathis, J. T., Merlivat, L., Millero, F. J., Monteiro, P. M. S., Munro, D. R., Murata, A., Newberger, T., Omar, A. M., Ono, T., Paterson, K., Pearce, D., Pierrot, D., Robbins, L. L., Saito, S., Salisbury, J., Schlitzer, R., Schneider, B., Schweitzer, R., Sieger, R., Skjelvan, I., Sullivan, K. F., Sutherland, S. C., Sutton, A. J., Tadokoro, K., Telszewski, M., Tuma, M., van Heuven, S. M. A. C., Vandemark, D., Ward, B., Watson, A. J., and Xu, S.: A multi-decade record of high-quality fCO2 data in version 3 of the Surface Ocean CO_2 Atlas (SOCAT), Earth Syst. Sci. Data, 8, 383–413, https://doi.org/10.5194/essd-8-383-2016, 2016.

Bentamy, A. and Fillon, D. C.: Gridded surface wind fields from Metop/ASCAT measurements, Int. J. Remote Sens., 33, 1729–1754, https://doi.org/10.1080/01431161.2011.600348, 2012.

Boccaletti, G., Ferrari, R., and Fox-Kemper, B.: Mixed Layer Instabilities and Restratification, J. Phys. Oceanogr., 37, 2228–2250, https://doi.org/10.1175/JPO3101.1, 2007.

Bourgault, D., Galbraith, P. S., and Chavanne, C. P.: Generation of internal solitary waves by frontally forced intrusions in geophysical flows, Nat. Comm., 7, 13606, https://doi.org/10.1038/ncomms13606, 2016.

Brüggemann, N. and Eden, C.: Evaluating Different Parameterizations for Mixed Layer Eddy Fluxes induced by Baroclinic Instability, J. Phys. Oceanogr., 44, 2524–2546, https://doi.org/10.1175/JPO-D-13-0235.1, 2014.

Capet, X., Roullet, G., Klein, P., and Maze, G.: Intensification of Upper-Ocean Submesoscale Turbulence through Charney Baroclinic Instability, J. Phys. Oceanogr., 46, 3365–3384, https://doi.org/10.1175/JPO-D-16-0050.1, 2016.

Capone, D. G. and Hutchins, D. A.: Microbial biogeochemistry of coastal upwelling regimes in a changing ocean, Nat. Geosci., 6, 711–717, https://doi.org/10.1038/ngeo1916, 2013.

Chaigneau, A., Gizolme, A., and Grados, C.: Mesoscale eddies off Peru in altimeter records: Identification algorithms and eddy spatio-temporal patterns, Prog. Oceanogr., 79, 106–119, https://doi.org/10.1016/j.pocean.2008.10.013, 2008.

Chavez, F. P., Takahashi, T., Cai, W.-J., Friederich, G., Hales, B., Wanninkhof, R., and Feely, R.: Coastal oceans, in: The First State of the Carbon Cycle Report (SOCCR): The North American Carbon Budget and Implications for the Global Carbon Cycle, edited by: King, A. W., Dilling, L., Zimmerman, G. P., Fairman, D. M., Houghton, R. A., Marland, G., Rose, A. Z., and Wilbanks, T. J., A report by the US Climate Change Science Program and the Subcommittee on Global Change Research, Washington, DC, 2007.

Colas, F., McWilliams, J. C., Capet, X., and Kurian, J.: Heat balance and eddies in the Peru-Chile current system, Clim. Dynam., 39, 509–529, https://doi.org/10.1007/s00382-011-1170-6, 2012.

Croquette, M., Eldin, G., Grados, C., and Tamayo, M.: On differences in satellite wind products and their effects in estimating coastal upwelling processes in the south-east Pacific, Geophys. Res. Lett., 34, L11608, https://doi.org/10.1029/2006GL027538, 2007.

Dale, A. C., Barth, J. A., Levine, M. D., and Austin, J. A.: Observations of mixed layer restratification by onshore surface transport following wind reversal in a coastal upwelling region, J. Geophys. Res.-Oceans, 113, C01010, https://doi.org/10.1029/2007JC004128, 2008.

Dickson, A. G., Sabine, C. L., and Christian, J. R., eds.: Guide to best practices for ocean CO_2 measurements, PICES Special Publication, 3, 191 pp., 2007.

Espinoza-Morriberón, D., Echevin, V., Colas, F., Tam, J., Ledesma, J., Váquez, L., and Graco, M.: Impacts of El Niño events on the Peruvian upwelling system productivity, J. Geophys. Res.-Oceans, 122, 5423–5444, https://doi.org/10.1002/2016JC012439, 2017.

Fairall, C. W., Bradley, E. F., Godfrey, J. S., Wick, G. A., Edson, J. B., and Young, G. S.: Cool-skin and warm-layer effects on sea surface temperature, J. Geophys. Res.-Oceans, 101, 1295–1308, https://doi.org/10.1029/95JC03190, 1996a.

Fairall, C. W., Bradley, E. F., Rogers, D. P., Edson, J. B., and Young, G. S.: Bulk parameterization of air-sea fluxes for Tropical Ocean-Global Atmosphere Coupled-Ocean Atmosphere Response Experiment, J. Geophys. Res.-Oceans, 101, 3747–3764, https://doi.org/10.1029/95JC03205, 1996b.

Ferrari, R.: A frontal challenge for climate models, Science, 332, 316–317, https://doi.org/10.1126/science.1203632, 2011.

Fox-Kemper, B., Ferrari, R., and Hallberg, R.: Parameterization of Mixed Layer Eddies, Part I: Theory and Diagnosis, J. Phys. Oceanogr., 38, 1145–1165, https://doi.org/10.1175/2007JPO3792.1, 2008.

Friederich, G. E., Ledesma, J., Ulloa, O., and Chavez, F. P.: Air-sea carbon dioxide fluxes in the coastal southeastern tropical Pacific, Prog. Oceanogr., 79, 156–166, https://doi.org/10.1016/j.pocean.2008.10.001, 2008.

Gruber, N.: Ocean biogeochemistry: Carbon at the coastal interface, Nature, 517, 148–149, https://doi.org/10.1038/nature14082, 2015.

Haine, T. W. N. and Marshall, J.: Gravitational, Symmetric, and Baroclinic Instability of the Ocean Mixed Layer, J. Phys. Oceanogr., 28, 634–658, https://doi.org/10.1175/1520-0485(1998)028<0634:GSABIO>2.0.CO;2, 1998.

Kao, T. W., Park, C., and Pao, H.-P.: Buoyant surface discharge and small-scale oceanic fronts: A numerical study, J. Geophys. Res., 82, 1747–1752, https://doi.org/10.1029/JC082i012p01747, 1977.

Köhn, E., Thomsen, S., Arévalo-Martínez, D. L., and Kanzow, T.: Underway measurements for 2-day upwelling front experiment during METEOR cruise M93, PANGAEA, available at: https://doi.org/10.1594/PANGAEA.881049, 2017.

Körtzinger, A., Mintrop, L., Wallace, D. W., Johnson, K. M., Neill, C., Tilbrook, B., Towler, P., Inoue, H. Y., Ishii, M., Shaffer, G., Torres Saavedra, R. F., Ohtaki, E., Yamashita, E., Poisson, A., Brunet, C., Schauer, B., Goyet, C., and Eischeid, G.: The international at-sea intercomparison of *f*CO_2 systems during the R/V Meteor Cruise 36/1 in the North Atlantic Ocean, Mar. Chem., 72, 171–192, https://doi.org/10.1016/S0304-4203(00)00080-3, 2000.

Landschützer, P., Gruber, N., and Bakker, D. C. E.: An updated observation-based global monthly gridded sea surface pCO_2 and air-sea CO_2 flux product from 1982 through 2015 and its monthly climatology (NCEI Accession 0160558), Version 2.2, NOAA National Centers for Environmental Information, Dataset, available at: https://www.nodc.noaa.gov/ocads/oceans/SPCO2_1982_2015_ETH_SOM_FFN.html, last access: 11 July, 2017.

Lapeyre, G. and Klein, P.: Impact of the small-scale elongated filaments on the oceanic vertical pump, J. Mar. Res., 64, 835–851, https://doi.org/10.1357/002224006779698369, 2006.

Laruelle, G. G., Lauerwald, R., Pfeil, B., and Regnier, P.: Regionalized global budget of the CO_2 exchange at the air-water interface in continental shelf seas, Global Biogeochem. Cy., 28, 1199–1214, https://doi.org/10.1002/2014GB004832, 2014.

Lefèvre, N. and Merlivat, L.: Carbon and oxygen net community production in the eastern tropical Atlantic estimated from a moored buoy, Global Biogeochem. Cy., 26, GB1009, https://doi.org/10.1029/2010GB004018, 2012.

Lefèvre, N., Guillot, A., Beaumont, L., and Danguy, T.: Variability of fCO_2 in the Eastern Tropical Atlantic from a moored buoy, J. Geophys. Res.-Oceans, 113, C01015, https://doi.org/10.1029/2007JC004146, 2008.

Lévy, M., Ferrari, R., Franks, P. J. S., Martin, A. P., and Rivière, P.: Bringing physics to life at the submesoscale, Geophys. Res. Lett., 39, L14602, https://doi.org/10.1029/2012GL052756, 2012.

Loginova, A. N., Thomsen, S., and Engel, A.: Chromophoric and fluorescent dissolved organic matter in and above the oxygen minimum zone off Peru, J. Geophys. Res.-Oceans, 121, 7973–7990, https://doi.org/10.1002/2016JC011906, 2016.

Mahadevan, A., Lévy, M., and Mémery, L.: Mesoscale variability of sea surface pCO_2: What does it respond to?, Global Biogeochem. Cy., 18, GB1017, https://doi.org/10.1029/2003GB002102, 2004.

Mahadevan, A., Tandon, A., and Ferrari, R.: Rapid changes in mixed layer stratification driven by submesoscale instabilities and winds, J. Geophys. Res., 115, C03017, https://doi.org/10.1029/2008JC005203, 2010.

McWilliams, J. C., Colas, F., and Molemaker, M. J.: Cold filamentary intensification and oceanic surface convergence lines, Geophys. Res. Lett., 36, L18602, https://doi.org/10.1029/2009GL039402, 2009.

Merlivat, L., Gonzalez Davila, M., Caniaux, G., Boutin, J., and Reverdin, G.: Mesoscale and diel to monthly variability of CO_2 and carbon fluxes at the ocean surface in the northeastern Atlantic, J. Geophys. Res., 114, C03010, https://doi.org/10.1029/2007JC004657, 2009.

Meyer, J., Löscher, C. R., Lavik, G., and Riebesell, U.: Mechanisms of P* Reduction in the Eastern Tropical South Pacific, Front. Mar. Sci., 4, 1–12, https://doi.org/10.3389/fmars.2017.00001, 2017.

Nash, J. D. and Moum, J. N.: River plumes as a source of large-amplitude internal waves in the coastal ocean, Nature, 437, 400–403, https://doi.org/10.1038/nature03936, 2005.

Nightingale, P. D., Malin, G., Law, C. S., Watson, A. J., Liss, P. S., Liddicoat, M. I., Boutin, J., and Upstill-Goddard, R. C.: In situ evaluation of air-sea gas exchange parameterizations using novel conservative and volatile tracers, Global Biogeoch. Cy., 14, 373–387, https://doi.org/10.1029/1999GB900091, 2000.

Ohman, M. D., Rudnick, D. L., Chekalyuk, A., Davis, R. E., Feely, R. A., Kahru, M., Kim, H.-J., Landry, M. R., Martz, T. R., Sabine, C. L., and Send, U.: Autonomous ocean measurements in the California Current Ecosystem, Oceanography, 26, 18–25, 2013.

Payne, R. E.: Albedo of the Sea Surface, J. Atmos. Sci., 29, 959–970, https://doi.org/10.1175/1520-0469(1972)029<0959:AOTSS>2.0.CO;2, 1972.

Peltier, W. R. and Caulfield, C. P.: Mixing efficiency in stratified shear flows, Annu. Rev. Fluid Mech., 35, 135–167, https://doi.org/10.1146/annurev.fluid.35.101101.161144, 2003.

Penven, P., Echevin, V., Pasapera, J., Colas, F., and Tam, J.: Average circulation, seasonal cycle, and mesoscale dynamics of the Peru Current System: A modeling approach, J. Geophys. Res., 110, C10021, https://doi.org/10.1029/2005JC002945, 2005.

Pierrot, D., Neill, C., Sullivan, K., Castle, R., Wanninkhof, R., Lüger, H., Johannessen, T., Olsen, A., Feely, R. A., and Cosca, C. E.: Recommendations for autonomous underway pCO_2 measuring systems and data-reduction routines, Deep-Sea Res. Pt. II, 56, 512–522, https://doi.org/10.1016/j.dsr2.2008.12.005, 2009.

Pietri, A., Echevin, V., Testor, P., Chaigneau, A., Mortier, L., Grados, C., and Albert, A.: Impact of a coastal-trapped wave on the near-coastal circulation of the Peru upwelling system from glider data, J. Geophys. Res.-Oceans, 119, 2109–2120, https://doi.org/10.1002/2013JC009270, 2014.

Ramachandran, S., Tandon, A., and Mahadevan, A.: Enhancement in vertical fluxes at a front by mesoscale-submesoscale coupling, J. Geophys. Res.-Oceans, 119, 8495–8511, https://doi.org/10.1002/2014JC010211, 2014.

Resplandy, L., Lévy, M., D'Ovidio, F., and Merlivat, L.: Impact of submesoscale variability in estimating the air-sea CO_2 exchange: Results from a model study of the POMME experiment, Global Biogeochem. Cy., 23, GB1017, https://doi.org/10.1029/2008GB003239, 2009.

Rudnick, D. L.: On the skewness of vorticity in the upper ocean, Geophys. Res. Lett., 28, 2045–2048, https://doi.org/10.1029/2000GL012265, 2001.

Shin, J., Dalziel, S., and Linden, P.: Gravity currents produced by lock exchange, J. Fluid Mech., 521, 1–34, https://doi.org/10.1017/S002211200400165X, 2004.

Smith, S. D.: Coefficients for sea surface wind stress, heat flux, and wind profiles as a function of wind speed and temperature, J. Geophys. Res.-Oceans, 93, 15467–15472, https://doi.org/10.1029/JC093iC12p15467, 1988.

Takahashi, T., Sutherland, S. C., Wanninkhof, R., Sweeney, C., Feely, R. A., Chipman, D. W., Hales, B., Friederich, G., Chavez, F., Sabine, C., Watson, A., Bakker, D. C., Schuster, U., Metzl, N., Yoshikawa-Inoue, H., Ishii, M., Midorikawa, T., Nojiri, Y., Körtzinger, A., Steinhoff, T., Hoppema, M., Olafsson, J., Arnarson, T. S., Tilbrook, B., Johannessen, T., Olsen, A., Bellerby, R., Wong, C., Delille, B., Bates, N., and de Baar, H. J.: Climatological mean and decadal change in surface ocean pCO_2, and net sea-air CO_2 flux over the global oceans, Deep-Sea Res. Pt. II, 56, 554–577, https://doi.org/10.1016/j.dsr2.2008.12.009, 2009.

Takahashi, T., Sutherland, S. C., Chipman, D. W., Goddard, J. G., Newberger, T., and Sweeney, C.: Climatological distributions of pH, pCO_2, total CO_2, alkalinity, and $CaCO_3$ saturation in the global surface ocean, ORNL/CDIAC-160, NDP-094, Carbon Dioxide Information Analysis Center, Oak Ridge National Laboratory, US Department of Energy, Oak Ridge, Tennessee, https://doi.org/10.3334/CDIAC/OTG.NDP094, 2014.

Taylor, J. R. and Ferrari, R.: Ocean fronts trigger high latitude phytoplankton blooms, Geophys. Res. Lett., 38, L23601, https://doi.org/10.1029/2011GL049312, 2011.

Thomas, L. N. and Lee, C. M.: Intensification of Ocean Fronts by Down-Front Winds, J. Phys. Oceanogr., 35, 1086–1102, https://doi.org/10.1175/JPO2737.1, 2005.

Thomas, L. N., Tandon, A., and Mahadevan, A.: Submesoscale Processes and Dynamics, in: Ocean Modeling in an Eddying Regime, edited by: Hecht, M. W. and Hasumi, H., American Geophysical Union, Washington, DC, https://doi.org/10.1029/177GM04, 2008.

Thomsen, S., Eden, C., and Czeschel, L.: Stability Analysis of the Labrador Current, J. Phys. Oceanogr., 44, 445–463, https://doi.org/10.1175/JPO-D-13-0121.1, 2014.

Thomsen, S., Kanzow, T., Colas, F., Echevin, V., Krahmann, G., and Engel, A.: Do submesoscale frontal processes ventilate the oxygen minimum zone off Peru?, Geophys. Res. Lett., 43, 8133–8142, https://doi.org/10.1002/2016GL070548, 2016a.

Thomsen, S., Kanzow, T., Krahmann, G., Greatbatch, R. J., Dengler, M., and Lavik, G.: The formation of a subsurface anticyclonic eddy in the Peru-Chile Undercurrent and its impact on the near-coastal salinity, oxygen, and nutrient distributions, J. Geophys. Res.-Oceans, 121, 476–501, https://doi.org/10.1002/2015JC010878, 2016b.

Ungarish, M. and Huppert, H. E.: On gravity currents propagating at the base of a stratified ambient, J. Fluid Mech., 458, 283–301, https://doi.org/10.1017/S0022112002007978, 2002.

Walter, R. K., Stastna, M., Woodson, C. B., and Monismith, S. G.: Observations of nonlinear internal waves at a persistent coastal upwelling front, Cont. Shelf Res., 117, 100–117, https://doi.org/10.1016/j.csr.2016.02.007, 2016.

Wanninkhof, R.: Relationship between wind speed and gas exchange over the ocean, J. Geophys. Res.-Oceans, 97, 7373–7382, https://doi.org/10.1029/92JC00188, 1992.

Wanninkhof, R.: Relationship between wind speed and gas exchange over the ocean revisited, Limnol. Oceanogr.-Meth., 12, 351–362, https://doi.org/10.4319/lom.2014.12.351, 2014.

Weiss, R. F.: Carbon dioxide in water and seawater: the solubility of a non-ideal gas, Mar. Chem., 2, 203–215, https://doi.org/10.1016/0304-4203(74)90015-2, 1974.

Weiss, R. F. and Price, B. A.: Nitrous oxide solubility in water and seawater, Mar. Chem., 8, 347–359, https://doi.org/10.1016/0304-4203(80)90024-9, 1980.

White, B. L. and Helfrich, K. R.: Rapid gravitational adjustment of horizontal shear flows, J. Fluid Mech., 721, 86–117, https://doi.org/10.1017/jfm.2013.41, 2013.